



Explicit algebraic Reynolds stress models for internal flows

1. Explicit algebraic models

Two explicit algebraic models are here compared in order to assess their predictive capabilities in the simulation of internal flow cases: a plane channel flow; a subsonic compressor cascade flow. The studied models are both coupled with a two-equations closure following the so-called effective viscosity concept. The turbulent velocity- and length-scale are determined by solving conservation equations for the turbulent kinetic energy (k) and the commonly used scalar turbulent dissipation rate (ϵ). In particular, the transport equation for the dissipation rate (ϵ) is implemented on the basis of the model proposed by Jones and Launder (1972).

The carried out numerical campaigns are limited to high-Reynolds number (HRN) flow regimes, thus the anisotropic turbulence closures under investigation are applied to the classical synthetic wall treatment. A detailed description of the adopted set of wall boundary conditions is given in section 4. Both the algebraic models are evaluated against the performance characteristics of the standard k - ϵ model proposed by Jones and Launder (1972), labeled as JL72.

The studied explicit algebraic models based on the weak-equilibrium assumption are:

- the explicit algebraic Reynolds stress model proposed by Gatski and Speziale (1993), labeled as GS93;
- the composite algebraic model in the formulation proposed by Jongen, Mompean and Gatski (1998), labeled as JMG98, which is based on the idea of coupling the algebraic stress and anisotropic dissipation rate formulations.

The models under investigation are not completely described here, whereas below is briefly commented the set of simplifications and assumptions used for their implementation.

2. The HRN implementation for the explicit algebraic models

The algebraic models are based on the contraction of Reynolds stress transport equation valid in equilibrium condition, for which convective and transport effects can be neglected. The complete Reynolds stress tensor τ_{ij} transport equation in non-inertial frame of reference reads as:

$$\frac{D\tau_{ij}}{Dt} = -\tau_{ik} \frac{\partial U_j}{\partial x_k} - \tau_{jk} \frac{\partial U_i}{\partial x_k} + \Pi_{ij} - \epsilon_{ij} - 2\Omega_m (e_{mkj}\tau_{ik} + e_{mki}\tau_{jk}) + D_{ij}^T + \nu \nabla^2 \tau_{ij}$$

where U_i is the mean velocity, e_{ijk} is the permutation tensor, Ω_m is the angular velocity, ν is the kinematic viscosity, Π_{ij} is the pressure-strain correlation, ϵ_{ij} is the dissipation rate tensor, and D_{ij}^T the turbulent transport term. Both the investigated models adopt the pressure-strain correlation proposed by Speziale, Sarkar and Gatski (1991) (SSG), that is tensorially linear in the stress anisotropy tensor $b_{ij} = (\tau_{ij} - (2/3)k\delta_{ij})/2k$, and reads as:

$$\Pi_{ij} = -C_1 \epsilon b_{ij} + C_2 k S_{ij} + C_3 k \left(b_{ik} S_{kj} + b_{jk} S_{ik} - \frac{2}{3} b_{mn} S_{mn} \delta_{ij} \right) + C_4 k (b_{ik} W_{jk} + b_{jk} W_{ik})$$

where $S_{ij} = 0.5(\partial U_i / \partial x_j + \partial U_j / \partial x_i)$, $\omega_{ij} = 0.5(\partial U_i / \partial x_j - \partial U_j / \partial x_i)$, and $W_{ij} = \omega_{ij} + e_{mji} \Omega_m$ are respectively the strain tensor, the relative and the absolute vorticity tensors. The model coefficients are:

$$C_1 = 3.4 + 1.8 P_k / \epsilon, \quad C_2 = 0.8 - 1.3 \Pi_b^{1/2}, \quad C_3 = 1.25, \quad C_4 = 0.4$$

with $\Pi_b = b_{ij} b_{ij}$.

2.1 EASM, GS93

The derivation of the algebraic formulation for the Reynolds stress is, in that case, based on the isotropic dissipation rate hypothesis. This means that the deviatoric part of the dissipation rate tensor is absorbed into the pressure-strain correlation: $\Pi_{ij} \approx \Pi_{ij} - D\varepsilon_{ij}$, which represents the only term able to account for any dissipation anisotropy. Using the SSG model and the isotropic dissipation rate hypothesis, the near-equilibrium form of the stress anisotropy tensor equation reads as:

$$b_{ij} = g\tau \left[-\alpha_1 S_{ij} - \alpha_2 (b_{ik}W_{jk} + b_{jk}W_{ik}) - \alpha_3 (b_{ik}S_{kj} + b_{jk}S_{ik} - (2/3)b_{mn}S_{mn}\delta_{ij}) \right],$$

with the following coefficients expression (Gatski and Speziale, 1993):

$$\alpha_1 = 0.5(1.33 - C_2), \quad \alpha_2 = 0.5(2 - C_4), \quad \alpha_3 = 0.5(2 - C_3), \quad g = (0.5C_1 + P_k/\varepsilon - 1)^{-1}, \quad \tau = k/\varepsilon.$$

The model is then completed by the transport equations for k and ε , written according to their general form (Jones and Launder, 1972):

$$\begin{aligned} \frac{Dk}{Dt} &= -\tau_{ij} \frac{\partial U_i}{\partial x_j} - \varepsilon + \frac{\partial}{\partial x_i} \left(\frac{v_T}{\sigma_k} \frac{\partial k}{\partial x_i} \right), \\ \frac{D\varepsilon}{Dt} &= -C_{\varepsilon 1} \frac{\varepsilon}{k} \tau_{ij} \frac{\partial U_i}{\partial x_j} - C_{\varepsilon 2} \frac{\varepsilon^2}{k} + \frac{\partial}{\partial x_i} \left(\frac{v_T}{\sigma_\varepsilon} \frac{\partial \varepsilon}{\partial x_i} \right), \end{aligned}$$

where:

$$v_T = C_\mu k^2/\varepsilon, \quad C_\mu = 0.09, \quad \sigma_k = 1, \quad \sigma_\varepsilon = 1.3, \quad C_{\varepsilon 1} = 1.44, \quad C_{\varepsilon 2} = 1.83.$$

The production-to-dissipation ratio is expressed by using the equilibrium expression proposed by Speziale (1991), formally valid for homogeneous turbulent flows, that reads as:

$$P_k/\varepsilon = (C_{\varepsilon 2} - 1)/(C_{\varepsilon 1} - 1)$$

According to the dissipation rate equation coefficients $C_{\varepsilon 1}$ and $C_{\varepsilon 2}$, the value imposed to the production-to-dissipation ratio is 1.89. Furthermore, the invariant Π_b is set equal to the universal equilibrium value predicted by the SSG model, $\Pi_b \approx 0.11$ (Gatski and Speziale, 1993).

2.2 Composite algebraic model, JMG98

The derivation of the composite model, instead, is based on the idea of coupling the algebraic stress formulation to a formally equivalent algebraic formulations of the dissipation rate tensor ε_{ij} . The Reynolds stress anisotropy now reads:

$$b_{ij} = \alpha_4 \tau \left[-\alpha_1 S_{ij} - \alpha_2 (b_{ik}W_{jk} + b_{jk}W_{ik}) - \alpha_3 (b_{ik}S_{kj} + b_{jk}S_{ik} - (2/3)b_{mn}S_{mn}\delta_{ij}) - d_{ij}/\tau \right],$$

The coefficients α_1 , α_2 and α_3 have the same expressions given in the GS93 model (Jongen, Mompean and Gatski, 1998), except from α_4 that is set: $\alpha_4 = g$.

The algebraic model of dissipation rate anisotropy d_{ij} leads to the following equation:

$$d_{ij} = -\frac{2g\varepsilon\tau}{15} C_{\mu\varepsilon}^* \left[S_{ij} + \beta_1 \tau (S_{ik}W_{kj}^* - W_{ik}^* S_{kj}) \right] \beta_2 \tau \left(S_{ik}S_{kj} - \frac{1}{3}S_{mn}S_{mn}\delta_{ij} \right)$$

where:

$$\begin{aligned} C_{\mu\varepsilon}^* &= \mathfrak{S}(g_\varepsilon \tau, W_{ij}, S_{ij}, \beta_1, \beta_2), \quad C_\omega^* = 81/26, \quad W_{ij}^* = \omega_{ij} + C_\omega^* e_{mji} \Omega_m, \\ \beta_1 &= g_\varepsilon 26/55, \quad \beta_2 = g_\varepsilon 8/11, \quad g_\varepsilon = (5.8 + P_k/\varepsilon - 1)^{-1} \end{aligned}$$

As far as the turbulent scales are concerned, the adopted k transport equation is used in its general formulation. Whereas the algebraic model for the dissipation rate anisotropy is coupled with a modified transport equation for the isotropic dissipation ε , that for HRN reads as:

$$\frac{D\varepsilon}{Dt} = -C_{\varepsilon 1}^* \frac{\varepsilon}{k} \tau_{ij} \frac{\partial U_i}{\partial x_j} - C_{\varepsilon 2} \frac{\varepsilon^2}{k} + \frac{\partial}{\partial x_i} \left(\frac{v_T}{\sigma_\varepsilon} \frac{\partial \varepsilon}{\partial x_i} \right),$$

with:

$$C_{\varepsilon 1}^* = \mathfrak{F}(C_{\varepsilon 1}, \beta_\varepsilon, d_{ij} S_{ij}, b_{ij} S_{ij}), \quad C_{\varepsilon 1}=1.0, \beta_\varepsilon=1.21, C_\mu=0.094, \sigma_\varepsilon=1.3.$$

Is here used a simplified linearized formulation for the JMG98 model. In such a formulation the pressure-strain term dependence from the production of kinetic energy is linearized about an equilibrium value of the production-to-dissipation ratio. The value for this ratio is again computed according to the equilibrium expression proposed by Speziale (1991), but using the coefficients appearing in the dissipation rate equation modelled by Jongen, Mompean and Gatski (1998). This assumption obviously leads to an internal inconsistency of the model, that could be considered a reasonable approximation in the limit of flow cases in near-equilibrium.



3. Numerical scheme

In the numerical flow simulations performed for the present study, the incompressible Navier-Stokes equations were solved by an original parallel inexact explicit non-linear Schwarz Domain Decomposition FEM scheme (Borello et al., 2000), briefly outlined in the following. The physics involved in the fluid dynamics of incompressible turbulent flows, in a non-inertial frame of reference, was modelled by Reynolds-Averaged Navier-Stokes (RANS) equations and discretised in space using a finite element weighted residual method. A strongly consistent stabilised PG scheme has been developed for turbomachinery CFD, that is able to control the instability origins affecting both the advective and diffusive incompressible flow limits (Corsini, 1996). The stabilisation was accomplished still in the context of weighted residual formulation thus preserving from the introduction of excessive numerical dissipation. It combines a Streamline Upwind/Petrov-Galerkin (SU/PG) treatment of model advective-diffusive equations with a Pressure Stabilising/Petrov-Galerkin (PS/PG) control of continuity equation. Both mixed-order Q2-Q1 or equal-order Q1-Q1 interpolation spaces are used for primary-turbulent and constraint variables, implicitly eliminating the undesirable pressure-checkerboarding effects. The FEM solution algorithm was based on an additive Schwarz DD method integrated in a Single Program Multiple Domain (SPMD) parallel concept. Data decomposition is carried out using an in-house made code developed to guarantee both the minimisation of the message passing requirements and the load balancing, and the MPI libraries were used for the message passing operations.

In particular, the numerical campaigns here presented have been carried out using the in-house developed finite element RANS solver with a Stabilized Petrov Galerkin formulation applied to mixed Q2-Q1 interpolation spaces (quadratic for primary-turbulent unknowns and linear for the corrected pressure). A preconditioned GMRes(50) algorithm is used as core sub-domain solver, and the convergence threshold has been set equal to 10^{-6} for both the solution errors and its residual.



4. Plane channel flow, problem statement

The flow is characterized by the following mean flow properties:

$$U_m = 1, \text{ mean bulk velocity}$$

$$U_c = 1.174 U_m, \text{ centreline velocity}$$

$$\delta = 1, \text{ channel half-width}$$

$$u_\tau = 0.0552, \text{ global wall shear-velocity}$$

$$Re_\tau = u_\tau \delta / \nu = 590, \text{ the friction Reynolds number}$$

$$Re_m = U_m 2\delta / \nu = 10800, \text{ the bulk Reynolds number}$$

The direct simulation of Moser et al. (1999) is regarded as highly accurate due to the very fine discretization level, and is here considered as a well-established reference solution for turbulence model assessment. This simulation has been chosen because it does not exhibit intense low-Reynolds number effects.

4.1 Plane channel flow, numerical model

Computational domain description

The computational domain models the half channel width δ , and it measures 100δ length along the axial direction that has been considered sufficient to establish the fully developed flow condition. Non-uniform finite element mesh across the flow field was used, and two discretization levels were tested. Respectively: a coarse mesh consisting of 3560 bi-quadratic elements, with use of 713 nodes in the axial direction (x), and 21 nodes in the direction normal to the solid boundary (y); a fine mesh of 7120 bi-quadratic elements obtained by doubling the nodes in the y direction.

The mesh anisotropy towards the solid boundary has been set in order to obtain the ensuing maximum y -to- x element aspect ratios 1:10 for the coarse mesh, and 1:20 for the fine mesh. The used stretching is able to fix, for both the meshes, the y^+ value on the first nodes row about 30 on the log-layer minor limit. In what follows, the plotted results refer to the coarse mesh because no meaningful differences were found during the carried out grid-dependency analysis.

Boundary conditions

The same set of boundary conditions was considered for the tested algebraic models. Dirichelet non-homogeneous boundary conditions were applied on the inflow section imposing uniform distributions for: the axial velocity component ($U=U_m$); the turbulent kinetic energy, computed on an inlet turbulence intensity set to 6%; the dissipation rate, modelled using a characteristic length scale set to 6% of the channel half-width δ .

The solid boundaries are, instead, treated with the wall-function. This permits to satisfy wall impermeability and to model the boundary layer action *via* the computation of a shear stress starting from a logarithmic velocity profile. Two models are here used to model the viscous region. The first model, labeled WFN, consists of the following equations:

$$U_t / u_\tau = \kappa^{-1} \ln(E y^+)$$

$$y^+ = y C_\mu^{1/4} k^{1/2} \rho / \mu$$

where U_t is the tangential velocity, u_τ is the shear velocity and y is the distance from the wall. The above specified eqs. lead to the evaluation of u_τ starting from k and U_t values computed at each preceding non-linear iteration. The values of constants are taken as: $E = 9$, $\kappa = 0.41$. While the coefficient C_μ is 0.09 for the *standard* k - ε model, and is specified in **section 2**. for the algebraic models. The set of wall boundary conditions is then completed by a homogeneous Neumann

condition on the turbulent kinetic energy ($\partial k / \partial n = 0$), and a Dirichlet value for the dissipation rate ($\varepsilon = C_\mu^{3/4} k^{3/2} / y$).

The second wall function model, labeled WFD, defines the shear velocity u_τ in terms of k so that the universal velocity profile reads as:

$$U_t = u_\tau \kappa^{-1} \ln(E u_\tau y / \nu)$$

In the above equation, the introduction of computed values of U_t permit to iteratively find the actual value of wall shear stress. In this model are imposed at the wall, Dirichlet boundary conditions for both the turbulent kinetic energy level, and the dissipation rate using the following relations:

$$k = \varepsilon C_\mu^{-1/2} (\overline{\partial u} / \partial y)^{-1}, \quad \varepsilon = C_\mu^{3/4} k^{3/2} / y$$

Neumann outflow conditions were enforced, which act as non-homogeneous integral on averaged momentum equation components introducing an additional traction. This set of boundary data originate from the Green-Gauss treatment of first-order non-linear Reynolds stress term appearing in the diffusive integral. Neumann homogeneous like conditions were, also, applied to the turbulence scaling variables.

4.2 Plane channel flow, numerical campaigns

The comparative investigation involved both integral as well as turbulent flow properties and quantities. Two WF models are used for the numerical campaigns. In the following are first commented the results obtained using the WFN, then the results of WFD are presented. Evident differences appear by comparing the two set of data (see in particular the average quantity fields), that could be in principle linked to the nature of boundary condition (Neumann vs. Dirichlet) applied to the turbulent kinetic energy in the viscous wall region ($y^+ < 50$).



4.3 Plane channel flow, results with WFN model

Integral flow properties

Table 1: Integral and mean flow properties

	DNS	JL72	GS93	JMG98
displacement thickness, δ^*/δ	0.141	0.049	0.061	0.054
momentum thickness, θ^*/δ	0.087	0.044	0.052	0.048
shape factor, H	1.182	1.114	1.173	1.125
ratio U_c/U_m	1.174	1.126	1.15	1.133
U^+ @ centreline	21.263	20.398	20.833	20.525

Data in Table 1, show clearly that the algebraic models, in the limit of their HRN implementation, are in sufficient agreement with the DNS velocity profile and in general they outperform the standard JL72 model. In detail the GS93 model agrees closely to the DNS data, as it is shown by its capability of predicting a correct profile shape H in the vicinity of the wall.

This means that the Reynolds number effect are correctly simulated although the use of a synthetic wall treatment.

Mean flow field data

The mean velocity distributions are plotted in Fig. 1 using linear scale and global coordinates, in Fig. 2 using semi-logarithmic scale and wall coordinates. While in Fig. 3 are plotted the turbulence kinetic energy profiles using global coordinates.

The following conclusions could be drawn:

1. In Fig. 1, the GS93 mean velocity profile agrees fairly with the DNS one, confirming the good prediction of mean velocity scales (U_c/U_m) shown in Table 1. In the vicinity of the wall the GS93 profile predicts also velocity gradient normal to the wall closer to the DNS one. Notwithstanding the whole HRN predictions fail in evaluating the physical shear stress level at the edge of the viscous layer.
2. In Fig. 2, the behaviour of computed U^+ profiles again confirm that the GS93 outperforms the other models in predicting the DNS distribution. This is particularly evident far from the wall starting from $y^+ = 100$.
3. In Fig. 3, the GS93 generally shows a fair agreement with DNS profile along the flow section. Nevertheless the GS93 k^+ centreline value is approximately twice the DNS one. Fig. 3 shows also that the GS93 model tends to predict on the wall the same k^+ level computed by JL72, whereas the JMG98 is capable of simulating a more realistic turbulent kinetic energy value. It is interesting to note, also, that the whole models are affected by the application of the wall Neumann condition on the turbulent kinetic energy that leads to an unphysical flattening of the predicted profiles.

Reynolds stress components

In Fig. 4.a, 4.b and 4.c the normal Reynolds-stresses are plotted, while in Fig. 5 the shear Reynolds stress profiles are shown. All the plotted distributions refer to global coordinates. The following conclusions could be highlighted:

4. In Fig. 4.a, the uu^+ profiles are compared. Again the algebraic models agree fairly to DNS data out of the viscous layer. Whereas in the vicinity of the wall (in the buffer layer about $y^+ = 30$) they under-predict the peak stress level. In Fig. 4.b, the vv^+ profiles are presented. Although the algebraic models over-predict the stress level along the flow section they outperform clearly the JL72 model. The same capacity is also confirmed comparing the ww^+ profiles shown in Fig.

- 4.c. The discussed figures show clearly the anisotropy in the normal Reynolds stresses recovered by the explicit algebraic models GS93 and JMG98.
5. In Fig. 5, the profiles of Reynolds shear stress are compared. Both the algebraic models demonstrate improved predicting capabilities. It is significant to note that the JMG98 model clearly outperforms the other ones showing a fair agreement with DNS data along the flow section. As far as the GS93 is concerned, it shows an over-prediction of Reynolds shear stress level in the vicinity of the wall, whereas it is able to predict a more realistic ‘effective’ viscosity starting from the log-law region.

Reynolds stress anisotropy

In Fig. 6 the Reynolds stress anisotropy components are presented for the algebraic models GS93 and JMG98. The plotted data show that, in the limit of the adopted case study, the two models predict very similar stress anisotropies along the channel section. In order to deepen the analysis in Table 2, the stress anisotropy components value computed at $y^+ = 100$ are compared against the DNS data supplied by Kim (1989), for $Re\tau = 395$, in the log-layer. The same table contains also data supplied by Wallin and Johansson (2000) for the same flow regime, using the GS93 model they have implemented. It is important to note that the computation carried out by Wallin and Johansson (2000) adopts a low-Reynolds number modelling.

Table 2: Reynolds stress anisotropy in the log-layer

	DNS $Re\tau = 395$ (Kim, 1989)	GS93 $Re\tau = 395$ (Wallin and Johansson, 2000)	GS93 $Re\tau = 590$	JMG98 $Re\tau = 590$
b_{11}	0.17	0.11	0.122	0.123
b_{22}	-0.13	-0.08	-0.091	-0.089
b_{12}	-0.18	-0.145	-0.146	-0.144

Non-equilibrium effects

The explicit algebraic models under investigation, although the near-equilibrium founding hypothesis, recover the capability of accounting to a certain extent for non-equilibrium flow effects. In order to discuss such a circumstance, in Fig. 7 the GS93 and JMG98 production-to-dissipation ratio distribution are compared. The plotted production-to-dissipation profiles, that are computed on the basis of the pressure-strain model linearized about an imposed equilibrium value of the ratio, are quite similar. Both the distributions are able to predict the existence of a region where the production balances the dissipation, located in the log-layer over the range of $y^+ = 120 \div 300$. Nevertheless the predicted ratios slightly differ from the DNS distribution (Moser et al., 1999), that has in the same region an opposite slowly increasing behaviour. In Table 3, the production-to-dissipation computed at $y^+ = 100$ and $y^+ = 300$ are compared to DNS data (Moser et al., 1999).

It is interesting to note that although the wrong distributions slope, both the GS93 and JMG98 profiles agree sufficiently with the DNS one in predicting the existence of an equilibrium in the log-law region. A second interesting analysis concerns with the behaviour of the scalar coefficient which multiplies the first order term in the non-linear stress tensor equation. This parameter could be interpreted as an effective turbulent viscosity defined as: $\nu_t^{eff} = C_\mu^{eff} k^2 / \epsilon$. The functional dependence $C_\mu^{eff} = \mathcal{J}(P_k/\epsilon)$ is analysed in Fig. 8 for the algebraic models GS93 and JMG98. Both the predicted functions agree with the experimental findings, indicating that the algebraic models

have the potential capability of predicting a boundary layer separation in adverse pressure gradient regions.

Table 3: Production-to-dissipation ratio distributions

	<i>DNS</i>	<i>GS93</i>	<i>JMG98</i>
P_k/ε at $y^+ = 100$	0.95	1.104	1.149
P_k/ε at $y^+ = 300$	0.95	1.02	1.003

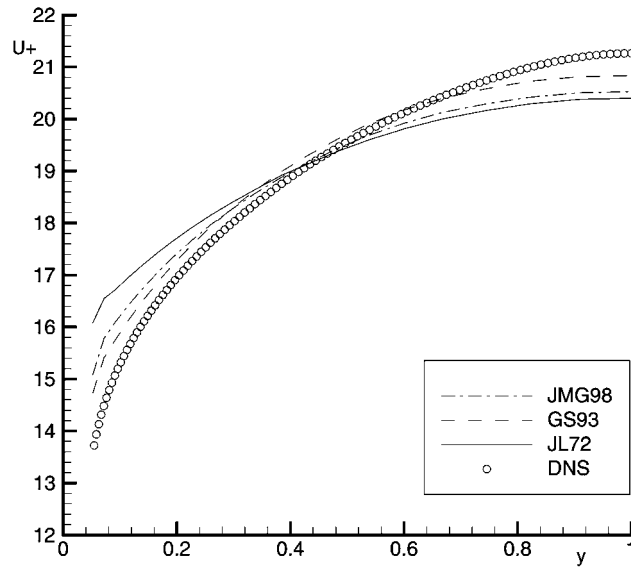


Fig. 1: Mean velocity profiles in global coordinates

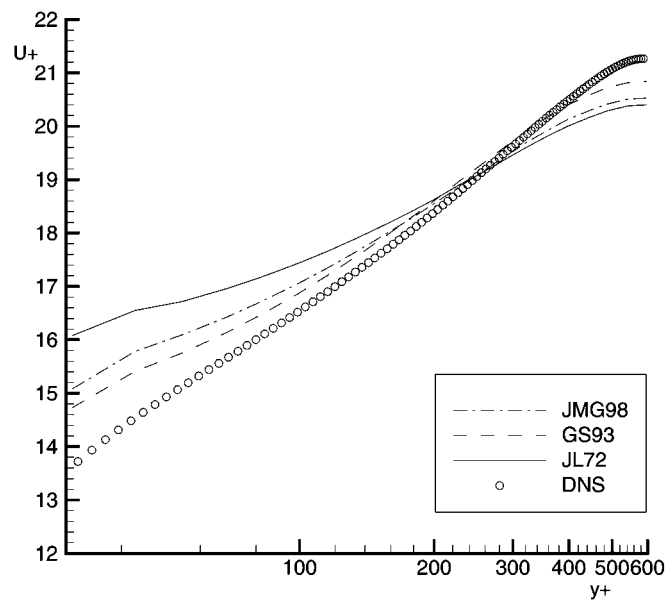


Fig. 2: Mean velocity profiles in semi-logarithmic scale and wall coordinates

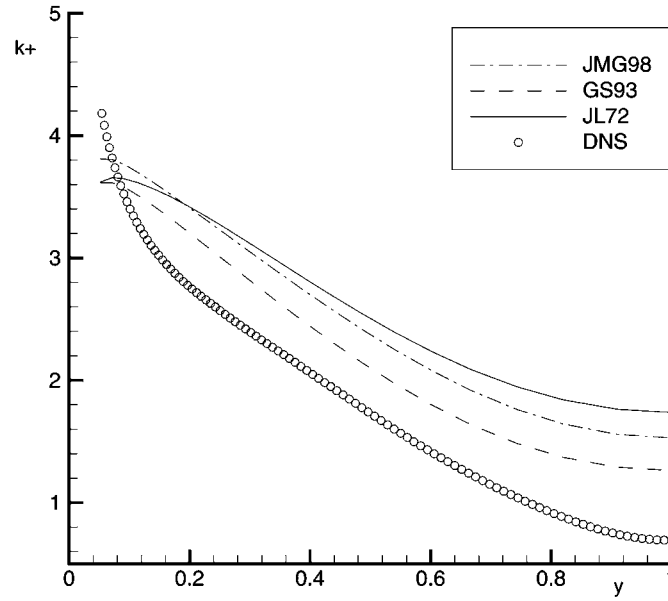


Fig. 3: Turbulent kinetic energy profiles in global coordinates

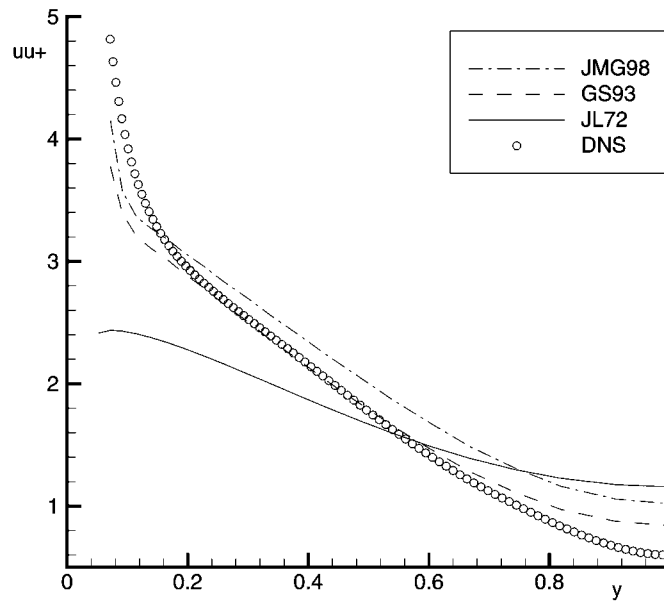


Fig. 4.a: Normal Reynolds stress (uu^+) in global coordinates

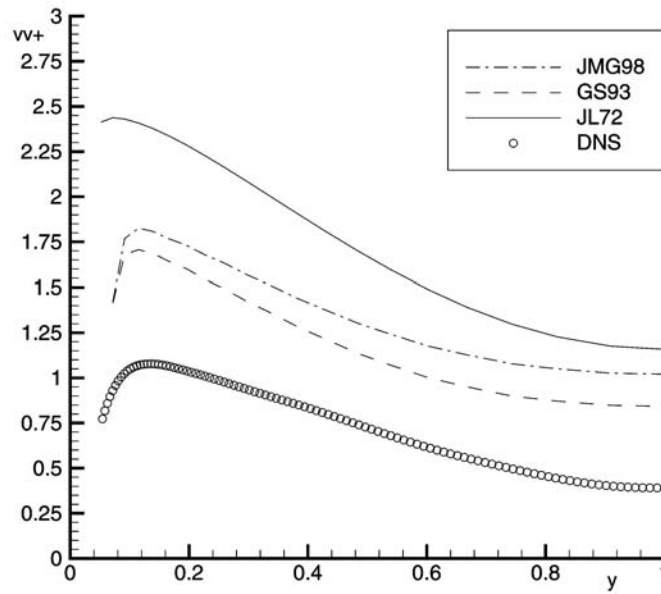


Fig. 4.b: Normal Reynolds stress ($v v^+$) in global coordinates

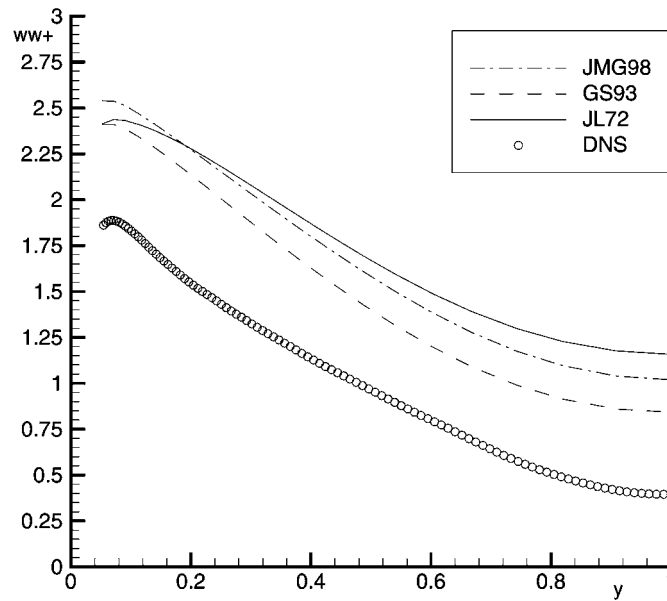


Fig. 4.c: Normal Reynolds stress ($w w^+$) in global coordinates

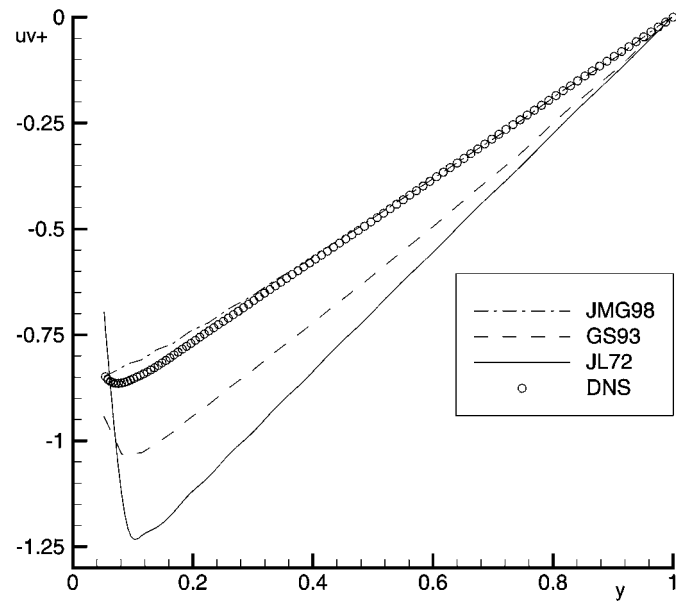


Fig. 5: Reynolds shear stress in global coordinates

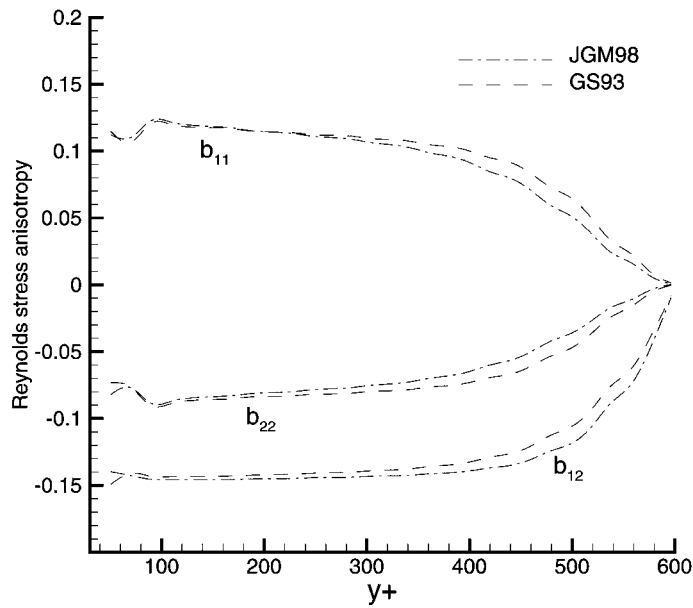


Fig. 6: Reynolds stress anisotropy in global coordinates

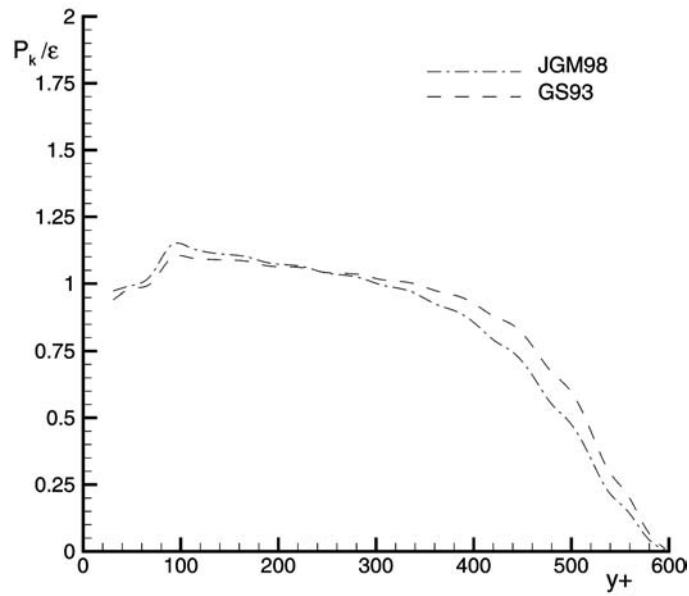


Fig. 7: Production-to-dissipation ratio in wall coordinates

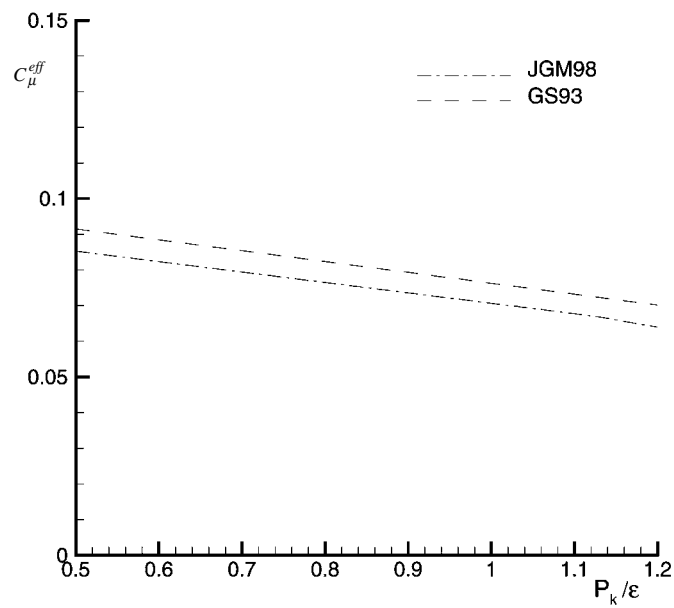


Fig. 8: C_μ^{eff} versus the production-to-dissipation ratio

4.4 Plane channel flow, results with WFD model

Integral flow properties

Table 4: Integral and mean flow properties

	DNS	JL72	GS93	JMG98
displacement thickness, δ^*/δ	0.141	0.071	0.078	0.0709
momentum thickness, θ^*/δ	0.087	0.0602	0.065	0.0598
shape factor, H	1.182	1.179	1.2	1.186
ratio U/U_m	1.174	1.16	1.179	1.159
U^+ @ centreline	21.263	21.015	21.359	21.015
U^+ @ $y^+ \cong 30$	13.722	13.522	13.156	13.335

Data in Table 4, show clearly that the use of WFD model improves, in the limit of the channel flow case, the whole models predicting capabilities. The whole predicted mean velocity field are similar and in good agreement with the DNS profile, as it is demonstrated by comparing the shape factor data. It is peculiar to note, also, that the WFD wall model permits to simulate the correct velocity gradient normal to the wall. For this reason an improved shear stress modelling is also expected.

Mean flow field data

The mean velocity distributions are plotted in Fig. 9 using linear scale and global coordinates, in Fig. 10 using semi-logarithmic scale and wall coordinates. While in Fig. 11 are plotted the turbulence kinetic energy profiles using global coordinates.

The following conclusions could be drawn:

9. In Fig. 9, the analysis carried out concerning the integral and mean flow properties (Table 4) are confirmed. In detail, near the wall the JL72 shows the best agreement with DNS, while both the algebraic models predict higher velocity defect about $y^+ = 30$. In the low-law region (y^+ ranging from 120 to 300) the tested models are in close agreement with the DNS data. Finally, close to the channel centreline the GS93 is the only model able to reach the correct velocity level.
10. In Fig. 10, the behaviour of computed U^+ profiles confirm the models capabilities. The three models clearly predict the existence of a so called ‘apparent’ log-law like region in the y^+ range 120 to 300, according to the classical theory for HRN channel flows.
11. In Fig. 11, the JMG98 profile, very similar to the JL72 one, is able to reach the k peak wall value closer to DNS. Whereas it predicts a higher kinetic energy level towards the channel centreline. Instead, the GS93 is able to simulate a realistic k profile starting from the log-law region (i.e. from $y \geq 0.2$), and it outperforms the other models as the channel centreline is approached.

Reynolds stress components

In Fig. 12.a, 12.b and 12.c the normal Reynolds-stresses are plotted, while in Fig. 13 the shear Reynolds stress profiles are shown. All the plotted distributions refer to global coordinates. The following conclusions could be highlighted:

12. In general the algebraic models predict normal stresses distributions which are in sufficient agreement to the DNS ones, outperforming the JL72 model. In Fig. 12.a, where the uu^+ profiles are compared, the JMG98 fits at the best with the DNS data except from y^+ ranging about 30 and 100. In Fig. 12.b and 12.c, presenting the vv^+ and ww^+ profiles, the GS93 predictions seem to be closer to the benchmark DNS data again far from the viscous region.
13. In Fig. 13, the profiles of Reynolds shear stress are compared. It is worth to note that GS93 distribution is significantly improved with respect to the WFN prediction (see Fig. 5). Both the

algebraic models are able of predicting a realistic shear stress distribution that is an ‘effective’ viscosity closer to the DNS computation. It is remarkable that in the vicinity of the buffer layer the JMG98 shear stress distribution is again closer to the DNS one.

Reynolds stress anisotropy

In Fig. 14 the Reynolds stress anisotropy components are presented for the algebraic models GS93 and JMG98. The plotted data show that, in the limit of the adopted case study, the two models predict similar stress anisotropies along the channel section with the GS93 able to predict more realistic level of stress anisotropy. In order to deepen the analysis in Table 2, the stress anisotropy components value computed at $y^+ = 100$ are compared against the DNS data supplied by Kim (1989) for $Re\tau = 395$, in the log-layer. The same table contains also data supplied by Wallin and Johansson (2000) for the same flow regime, concerning the GS93 model they have implemented. It is important to note that the computation carried out by Wallin and Johansson (2000) adopts a low-Reynolds number modelling.

Table 5: Reynolds stress anisotropy in the log-layer

	<i>DNS</i> <i>Reτ = 395</i> <i>(Kim, 1989)</i>	<i>GS93</i> <i>Reτ = 395</i> <i>(Wallin and Johansson, 2000)</i>	<i>GS93</i> <i>Reτ = 590</i>	<i>JMG98</i> <i>Reτ = 590</i>
b_{11}	0.17	0.11	0.1097	0.1088
b_{22}	-0.13	-0.08	-0.08	-0.0077
b_{12}	-0.18	-0.145	-0.143	-0.14

Non-equilibrium effects

In Fig. 15 the GS93 and JMG98 production-to-dissipation ratio distributions are compared. The plotted production-to-dissipation profiles, that are computed on the basis of the pressure-strain model linearized about an imposed equilibrium value of the ratio, are quite similar. Both the distributions are able to predict the existence of a region where the production balances the dissipation, located in the log-layer over the range of $y^+ = 120 \div 300$. Furthermore, seems to be predicted correctly also the slowly increasing behaviour that characterizes the DNS distribution in that region (Moser et al., 1999). In Table 6, the production-to-dissipation computed at $y^+ = 100$ and at $y^+ = 300$ are compared to DNS data (Moser et al., 1999).

Table 6: Production-to-dissipation ratio distributions

	<i>DNS</i>	<i>GS93</i>	<i>JMG98</i>
$P_k\varepsilon$ at $y^+ = 100$	0.95	1.036	0.898
$P_k\varepsilon$ at $y^+ = 300$	0.95	1.134	1.051

The second non-equilibrium feature is the functional dependence $C_\mu^{eff} = \mathfrak{I}(P_k/\varepsilon)$, that is analysed in Fig. 16 for the algebraic models GS93 and JMG98. As already shown for WFN wall model, both the predicted functions agree with the experimental findings.

References

- Borello, D., Corsini, A., and Rispoli, F., A finite element overlapping scheme for turbomachinery flows on parallel platforms. submitted to *Computer and Fluids* (MS#00-145), 2000.
- Corsini, A., *3D analysis of Francis turbine runner: performance prediction using a finite element technique with unassembled stiffness matrix treatment* (in Italian). Doctoral Thesis, 1996, DMA - University of Rome "La Sapienza".
- Gatski, B.T., and Speziale, C. G., On explicit algebraic stress models for complex turbulent flows, *J. Fluid Mech.*, **254**, 1993, 59-78.
- Jongen, T., Mompean, G., and Gatski, B.T., Accounting for Reynolds stress and dissipation rate anisotropies in inertial and non-inertial frames, *Phys. Fluids*, **10**, 1998, 674-684.
- Jones, W.P., and Launder, B.E., The prediction of laminarization with a two-equation model of turbulence, *Int. J. of Heat Mass Transfer*, **15**, 1972, 301-314.
- Kim, J., On the structure of pressure fluctuations in simulated turbulent channel flow, *J. Fluid Mech.*, **205**, 1989, 421-451.
- Moser, R.D., Kim, J., and Mansour, N.M., Direct numerical simulation of turbulent channel flow up to $Re_\tau = 590$, *Phys. Fluids*, **11**, 1999, 943-945.
- Speziale, C.G., Analytical methods for the development of Reynolds stress closures in turbulence, *Ann. Rev. Fluid Mech.*, **23**, 1991, 107-157.
- Speziale, C.G., Sarkar, S., and Gatski, B.T., Modeling the pressure-strain correlation of turbulence: an invariant dynamical systems approach, *J. Fluid Mech.*, **227**, 1991, 245-272.
- Wallin, S., and Johansson, A.V., An explicit algebraic Reynolds stress model for incompressible and compressible turbulent flows, *J. Fluid Mech.*, **403**, 2000, 89-132.

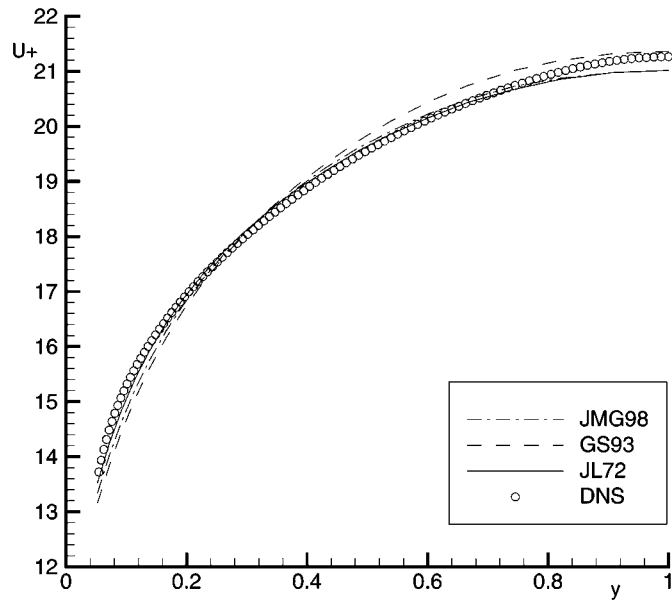


Fig. 9: Mean velocity profiles in global coordinates

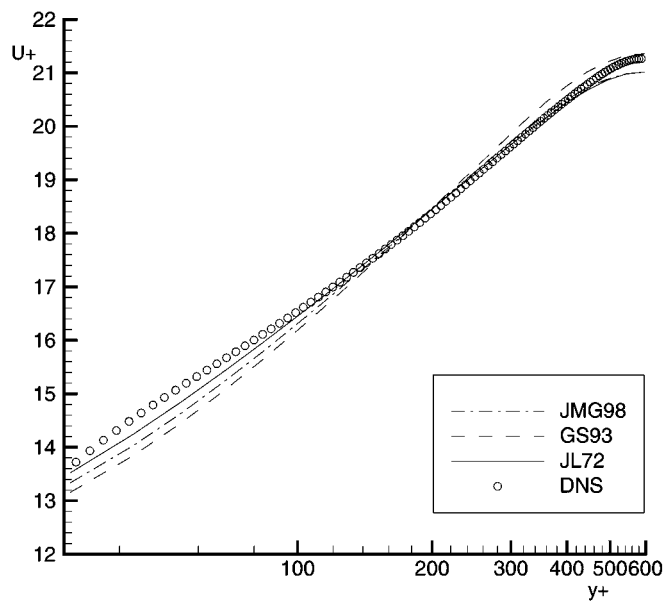


Fig. 10: Mean velocity profiles in semi-logarithmic scale and wall coordinates

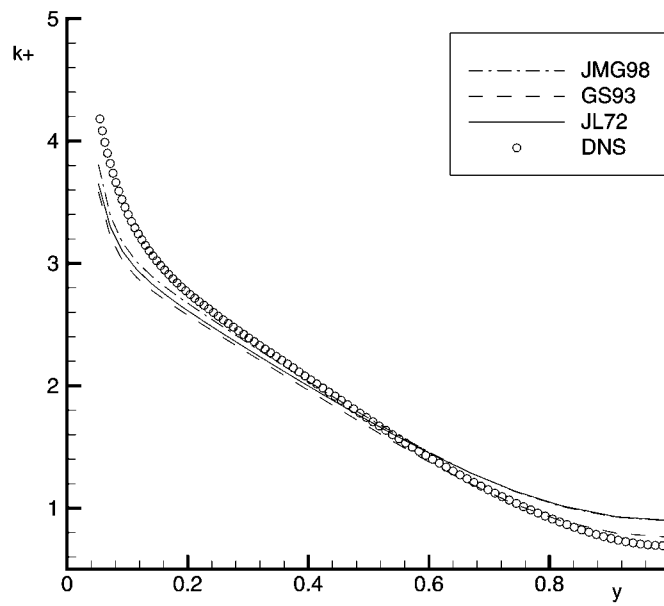


Fig. 11: Turbulent kinetic energy profiles in global coordinates

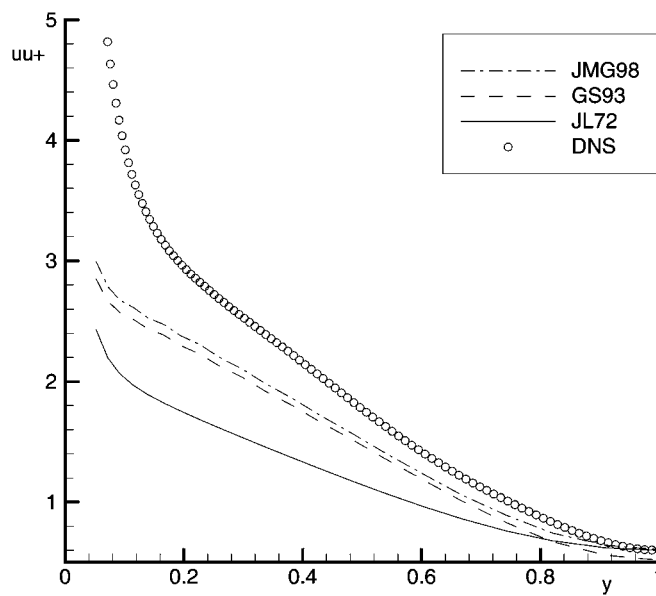


Fig. 12.a: Normal Reynolds stress (uu^+) in global coordinates

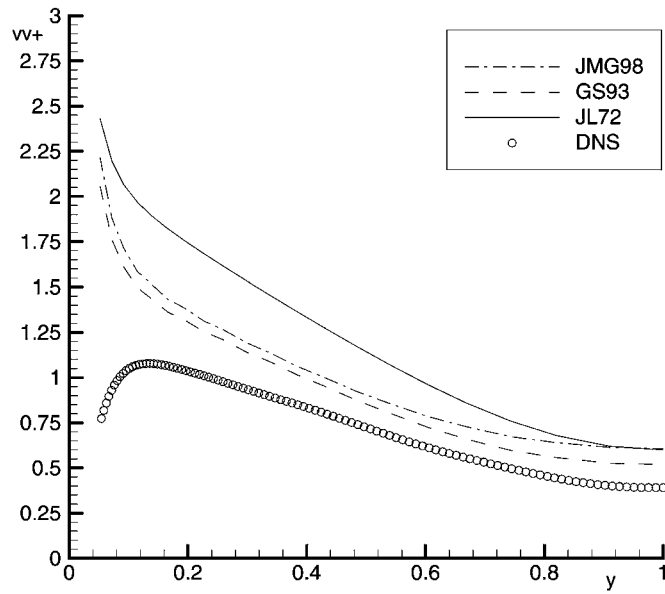


Fig. 12.b: Normal Reynolds stress (vv^+) in global coordinates

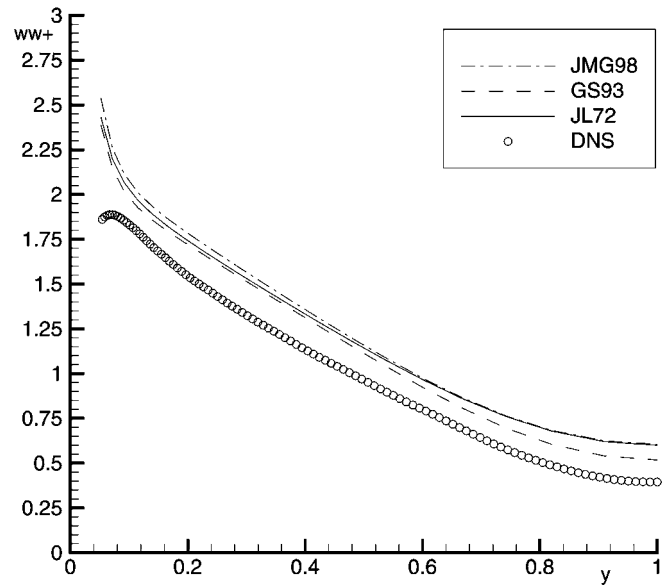


Fig. 12.c: Normal Reynolds stress (ww^+) in global coordinates

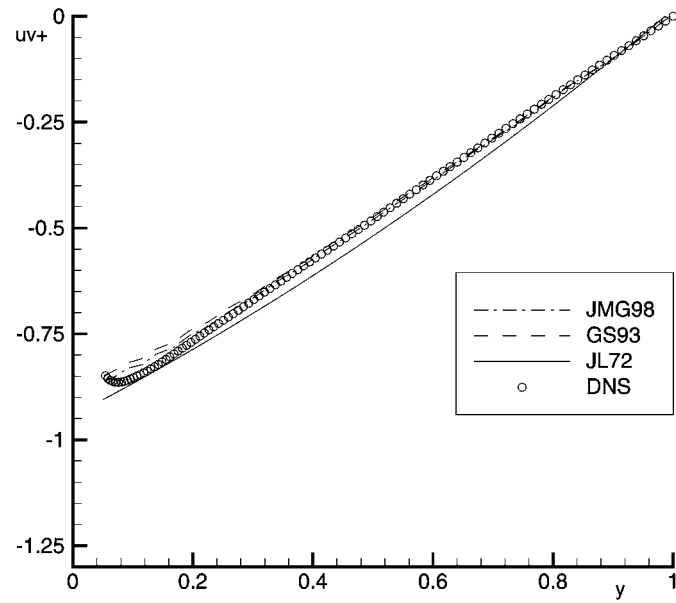


Fig. 13: Reynolds shear stress in global coordinates

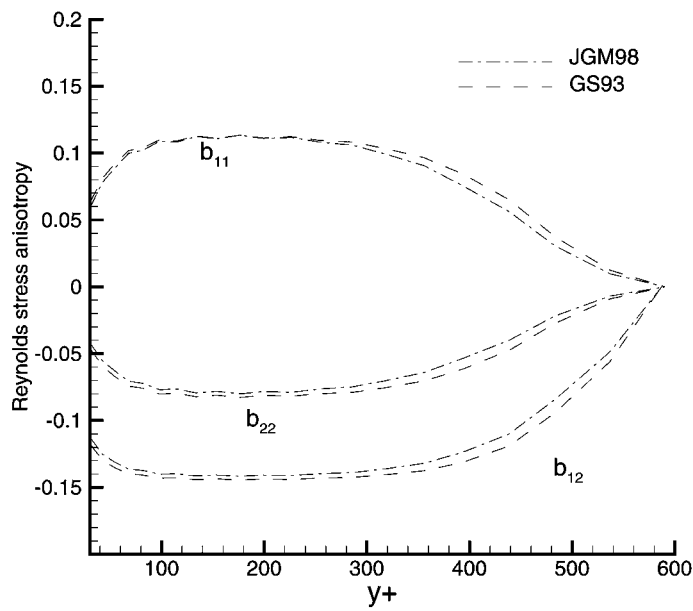


Fig. 14: Reynolds stress anisotropy in global coordinates

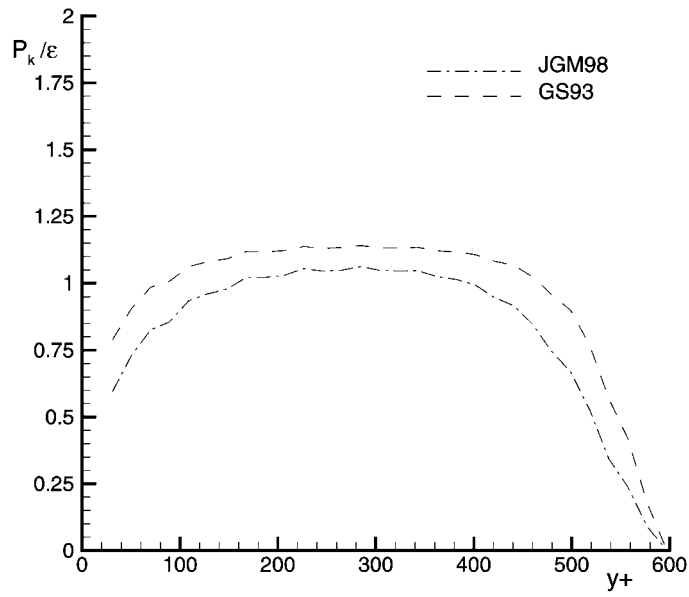


Fig. 15: Production-to-dissipation ratio in wall coordinates

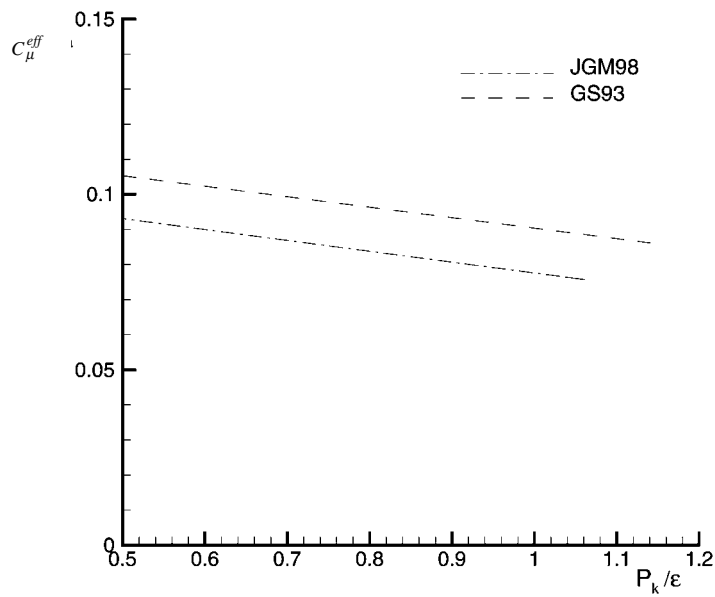


Fig. 16: C_μ^{eff} versus the production-to-dissipation ratio